Proceedings of the 10th World Congress on Momentum, Heat and Mass Transfer (MHMT 2025)
Barcelona, Spain - April, 2025
Paper No. CSP 133
DOI: 10.11159/csp25.133

Proper Orthogonal Decomposition of Liquid Jet Breakup Dynamics in Annular Crossflow

Deepak Kumar[1], Abhishek Verma[1], Abhijit Kushari[1]
[1]Indian Institute of Technology Kanpur
Department of Aerospace Engineering, Kanpur, India
deepakkr@iitk.ac.in; abhishv@iitk.ac.in; akushari@iitk.ac.in

***Abstract* -** The primary breakup of a liquid jet in an annular passage under a crossflow of air at a fixed Mach number of 0.12 and atmospheric pressure is experimentally analyzed. The study covers liquid jet velocities from 1.417 m/s to 7.084 m/s (orifice diameter = 1 mm), corresponding to liquid-air momentum flux ratios between 1 and 25. Proper Orthogonal Decomposition (POD) is utilized to investigate coherent structures, energy distribution, and temporal evolution at varying momentum flux ratios (q).
High-speed imaging at 3000 fps is performed, and 3000 images are processed for POD analysis. The findings reveal that lower q leads to early turbulence dominated by shear-layer instabilities, while higher q delays turbulence onset due to persistent vortex roll-up. Energy spectrum analysis confirms that the first 10 POD modes capture the dominant flow structures, while temporal analysis demonstrates a transition from crossflow-dominated turbulence at low q to self-sustained turbulence at high q.

***Keywords*:** POD, Jet in Cross-flow, High speed imaging, Primary breakup

1. Introduction

The primary breakup process of a liquid jet in crossflow is encountered in various applications, including air-breathing propulsion systems, liquid rocket engines, diesel engines, spark ignition engines, and agricultural sprays. The operation of gas turbines, diesel, and gasoline engines relies on the injection of liquid fuel in the form of fine droplets. The atomization process, which increases the total surface area of the fuel, significantly influences vaporization rates, combustion efficiency, and NOx emissions. Consequently, understanding the atomization process is essential for optimizing air/fuel mixing, spatial distribution of liquid drops, and vaporization rates.

In spray formation studies, it is crucial to understand the mechanisms governing liquid jet breakup, including penetration height, droplet size distribution, and spray dispersion. One of the primary goals in modern combustion systems is the reduction of harmful NOx emissions from aircraft engines. One effective strategy is to prevent hot spots in combustors by achieving a lean, homogeneous fuel-air mixture upstream of the combustor inlet. Proper understanding of atomization mechanisms aids in reducing emissions and enhancing efficiency. Moreover, these insights are crucial for validating Computational Fluid Dynamics (CFD) models, which are increasingly used to optimize fuel injection processes. Fine atomization and precise fuel placement play a pivotal role in achieving high mixing efficiency, with liquid jets in crossflow meeting these requirements effectively. Therefore, understanding primary breakup dynamics and drop distribution inside a spray remains a key research challenge.

Wu et al. [1] studied the penetration and surface breakup processes of liquid jets in crossflows, demonstrating that liquid columns fracture at a constant streamwise location. They inferred drag coefficients from column trajectories, noting a weak dependence on liquid viscosity. Their findings correlated fracture height with the time required for an analogous droplet to complete secondary breakup. The disintegration of liquid jets by axisymmetric waves has also been investigated theoretically and experimentally [2]. Wu, Fuller, and Kirkendall [3] measured droplet size, axial velocity, and volume flux across the spray plume at various downstream locations. Their observations revealed a concave layered droplet distribution at high momentum flux ratios, where large droplets were concentrated at the plume top and volume flux peaked along the spray centerline. The study highlighted that liquid mass distribution is non-uniform, with the majority of droplets located in the upper spray region at high momentum flux ratios.

Several researchers, including Wu et al. [3], Vich [4], and Mazallon et al. [5], have classified primary breakup regimes in liquid jets in crossflow. These regimes—bag, multimode, and shear breakup—closely resemble the secondary breakup of individual droplets. Wu et al. [1] developed a breakup regime map based on Weber number and momentum flux ratio, reporting that the cross-stream breakup location for all three breakup modes was constant at approximately eight jet diameters, while the streamwise breakup location depended on momentum flux ratio. Mazallon et al. [4] further demonstrated that for low Ohnesorge numbers, crossflow Weber number alone governs breakup transitions and proposed an updated breakup regime map incorporating both Weber number and Ohnesorge number. Sallam et al. [6] refined the transition boundary between bag and multimode breakup regimes, showing that the breakup time remained constant at 2.5 t* across different Weber numbers for low-Ohnesorge-number jets. They also analyzed ligament formation, drop velocities, and breakup rates for multimode and shear breakup modes, though bag breakup was not examined in detail.

Kush and Schetz [7] studied liquid jet injection in supersonic crossflows, identifying three breakup regimes based on momentum flux ratio (q). At low q (<4), jet breakup is dominated by wave instabilities on the liquid column. At moderate q (~11), wave growth and droplet shedding become dominant, with droplets gradually dispersing along the fracture point. Ingebo [8] classified these waves as capillary and acceleration waves, describing atomization as a process where ligaments form at the crest of column waves. Schetz and Padhye [9] performed a momentum balance analysis to predict maximum jet penetration height, correlating it with momentum flux ratio (q). Their findings showed that penetration height increases until the liquid momentum is fully redirected into the airstream.

Nejad and Schetz [10] analyzed the effects of liquid properties on jet breakup in supersonic crossflows, demonstrating that surface tension has minimal impact on penetration height but significantly influences jet breakup rate and droplet size. Chen et al. [11] used Mie scattering to track jet trajectories and categorized spray formation into three distinct regimes: liquid column, ligament, and droplet regimes. Velocity measurements obtained via Particle Image Velocimetry (PIV) revealed droplet trajectories and boundary layer interactions. Thomas and Schetz [12] further examined spray characteristics in supersonic airstreams, analyzing droplet size distribution, penetration profiles, and mass flux distributions.

Sankarakrishnan and Sallam [13] studied column and surface waves in non-turbulent liquid jets undergoing bag breakup, explaining the formation of three distinct droplet sizes based on membrane rupture, ring string fragmentation, and ring node detachment. Their results reinforced the importance of Rayleigh-Taylor instability in governing jet breakup behavior.

Over the years, extensive research has been conducted to identify various flow patterns using computational, experimental, and signal processing techniques. Advances in optical diagnostics have enabled high-frame-rate imaging of liquid jet breakup, yet challenges remain due to the microscopic scales involved. Proper Orthogonal Decomposition (POD) has emerged as a powerful tool for extracting meaningful insights from these complex datasets. Introduced to fluid mechanics by Lumley [14], POD is widely used for analyzing coherent structures in turbulence. Sirovich [15] developed the snapshot POD method, which decomposes instantaneous flow snapshots into orthogonal modes to characterize dominant flow structures. Bernero and Fiedler [16] successfully combined PIV and POD to study spray dynamics, and similar approaches have been applied to analyzing liquid jet breakup [17].

The application of POD to jet breakup studies continues to provide deeper insights into turbulent energy distribution, coherent structure dynamics, and atomization efficiency. With advancements in high-speed imaging and computational modeling, ongoing research aims to refine breakup regime predictions, improve combustion efficiency, and develop low-emission fuel injection strategies

2. Experimental setup and Methodology

The benchmarking of the overall experiment setup is shown in figure 2.6. The overall experimental setup is assembled mainly by three parts-air supply system, water supply system and test section. The air supply system consists of centrifugal blower. The centrifugal blower is connected to settling chamber through a steel flexible tube while the two-stage axial compressor is connected to high pressure tank with an iron pipe. The test section consists of a high-pressure chamber having a glass tube fixed at the centre which has an inner stainless-steel tube with 1 mm diameter orifice. The water from the water supply system injected perpendicular to the free stream of air through 1 mm diameter orifice. The water supply system consists of a steel water tank filled with water. The water is pressurized from the air compressor. The air from the blower goes to settling chamber via flexible steel tube. Thereafter it goes to the main test section through an iron pipe. For high pressure experiment, the compressed air from two stage axial compressor travels via an iron pipe of 60 mm diameter to high pressure tank. From pressure tank, the air goes to glass tube via steel pipe by passing through swirl vane which is adjusted just before entering the glass. The air inlet velocity is measured using a pitot tube fixed above the swirl vane. The pitot tube is then connected to a micro manometer to display air velocity or differential pressure sensors to display and record the measured velocity with the help of LabVIEW program. To measure the inlet temperature, a thermocouple is fixed in a steel pipe at some distance above from the swirl vane. One gage pressure sensor is connected to the upper lid of high-pressure chamber to measure and indicate the static pressure of pressure chamber and other is connected to the iron pipe to measure and indicate static pressure of flow. The water from the outlet of tank flow through turbine flow meter to measure volume flow rate of water. The required flow rate of water is controlled by controlling tab and flow regulator. The pressure inside the water tank is control by the pressure knob. A dial gauge is used to control and monitor the pressure of the tank. The air stream interacts with horizontally injected water jet. It bends and breaks jet into large number of ligaments and droplets of different sizes. The breakup phenomenon occurring in the test section and droplets sizes and velocities distribution is done by high-speed imaging and PDPA measurement.

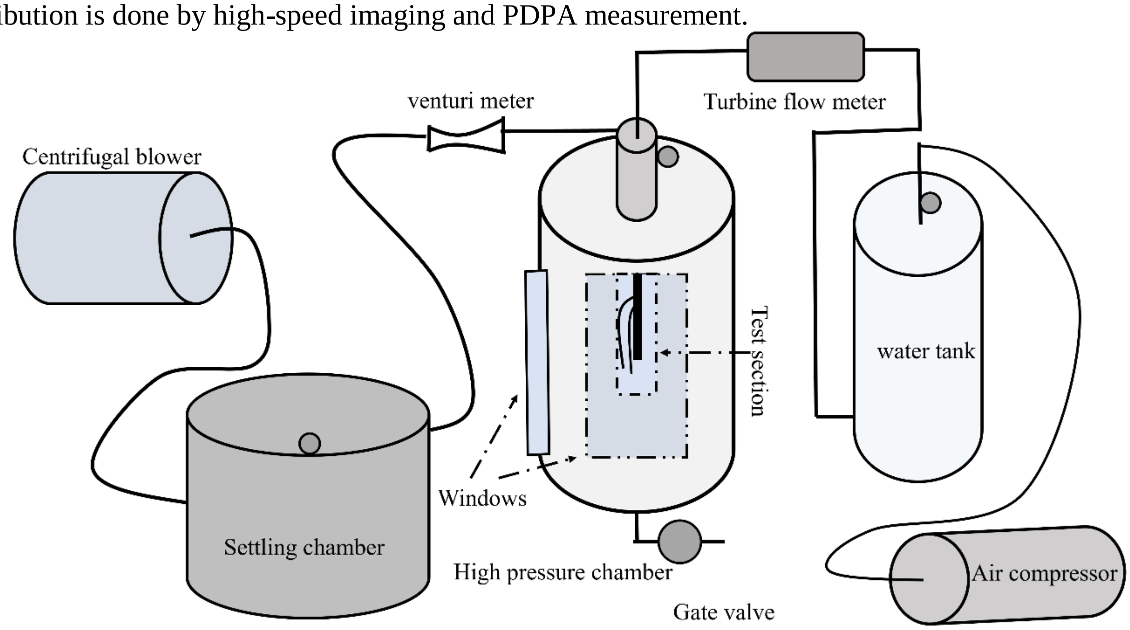

Fig. 1. Schematic diagram of the experimental setup.

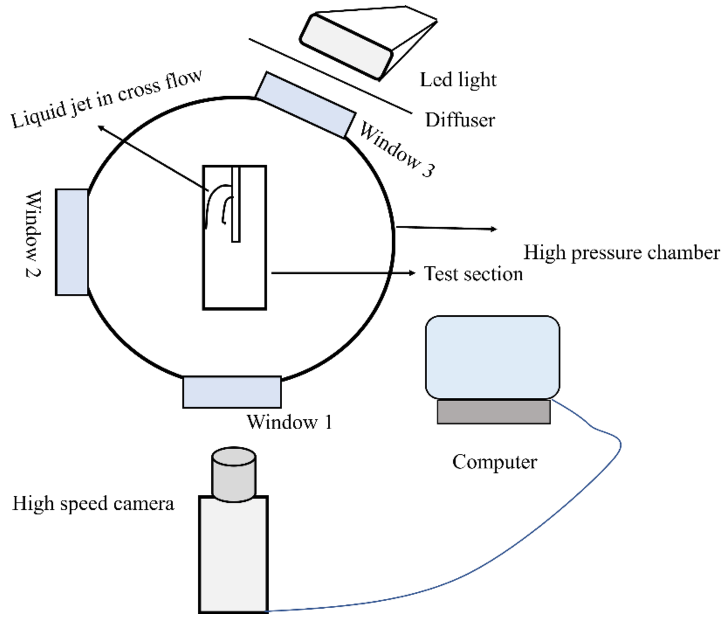

Fig. 2. High Imaging setup for jet in cross flow.

2.1. Test Conditions

All experiments are conducted at room temperature. Water is used as a working fluid. The diameter of the orifice in which water is horizontally injected perpendicular to cross stream is 1mm. The inlet temperature is 303 K. The momentum flux ratio (q) varies from 3 to 25. The air inlet Mach number (M) in vertical downward direction is kept constant (M = 0.12) as air inlet velocity is also constant which is equal to 42 m/s (U_∞=42 m/s). At atmospheric condition, the density of air, ρ =1.16 kg/m3, the Aerodynamic Weber number (We) = 28 (based on jet diameter of 1mm), the air Reynolds number Re = 45245.7(based on passage height of r2-r1 =17.5) and air mass flow rate, $\dot{m}$ = 0.1044 kg/s. In a cross flow, the air inlet velocity is same as free stream velocity ($U=U_\infty$). Water jet velocity varied from 1.4 to 7.1 ms-1 as momentum flux ratio (q) varied from 1 to 25 while keeping air velocity constant (U=42 ms-1). The volume flow rate of water corresponds to the velocity range in Q =65 to 336 mLPM. The liquid dimensionless number, that is, Reynolds number and Weber number are respectively varied from 1416.839 to 7074.194 and 28 to 698. But the Ohnesorge number for water at room temperature is very small and equals to 0.004 (which is very less than 0.01). So, the effect of Ohnesorge number on liquid jet breakup is very negligible.

2.2. High Speed Imaging and Processing

The disintegration of liquid jet is caused by aerodynamic force. These waves develop on the liquid surface, increase in their amplitude and loss of stability. Due to this penetration height, penetration distance and breakup locations are time dependent and different for each image of the same momentum flux ratio. The images are captured at 3000 fps (3000 sample per second) at an exposure time 40 µs and 3000 images are saved for 1 second. Each temporal image was processed and analyzed using Matlab software. An average of 3000 images is used to represent the average height, length, and breakup locations. Penetration height, distance and break-up location are the major important parameters in primary break-up of liquid jet. Breakup location is defined as the point of continuous liquid jet column where it disintegrates into ligaments and droplets. Penetration height is defined as the maximum transverse distance travels by column of liquid jet up-to breakup zone. The spray snapshots were captured using a 4M Phantom V341 high-speed camera. To analyze the high-speed images, they were first processed using MATLAB. The preprocessing involved background subtraction, followed by cropping to a smaller region. Background subtraction effectively removes unwanted noise, enhancing the clarity of the spray features for further analysis. The images were then cropped to a fixed size of 240 pixels along the spray direction and 240 pixels across (240 × 240) to ensure that the spray remained well within the selected region. The resulting images were subsequently used as input for Proper Orthogonal Decomposition to extract coherent structures within the spray.

2.3. Proper orthogonal decomposition

The Proper Orthogonal Decomposition (POD) is a well-established mathematical technique widely used to identify coherent structures embedded within a flow. The snapshot-based approach to POD involves collecting an ensemble of snapshots from either experimental measurements or numerical simulations and using them to generate a set of basic functions that span the dataset. In this analysis, intensity snapshots of the spray are utilized. The first step is to compute the mean spray image, which represents the zeroth mode of POD. The subsequent analysis focuses on the fluctuating component of the spray intensity relative to this mean image.

Each snapshot is essentially a 2D matrix, where each cell corresponds to the intensity value of a specific pixel in the spray image. For a snapshot of m × n pixels, there are a total of mn intensity values. These intensity values, obtained from N snapshots, are then arranged into a matrix U, which serves as the input for the POD analysis.

$$U = [u^1 \; u^2 \; u^3 \; \ldots \ldots u^N] \tag{1}$$

$$U = \begin{bmatrix} u_1^1 & u_1^2 & \ldots u_1^N \\ u_2^1 & u_2^2 & \ldots u_2^N \\ & \vdots & \\ u_{mn}^1 & u_{mn}^2 & \ldots u_{mn}^N \end{bmatrix} \tag{2}$$

The auto-covarince matrix is then created as

$$\tilde{C} = U^T U \tag{3}$$

And the corresponding eigenvalue problem

$$\tilde{C} A^i = \lambda^i A^i \tag{4}$$

is solved. For convenience, the eigenvectors are ordered according to the magnitude of the eigenvectors

$$\lambda^1 > \lambda^2 > \lambda^3 \cdots \lambda^N = 0 \tag{5}$$

For convenience, the eigenvectors are normalized. The eigenvectors of (3.3) make up a basis for the construction of POD modes $\phi^{'}$,

$$\phi^{'} = \sum_{p=1}^{N} A_p^i u^p \bigg/ \left\| \sum_{p=1}^{N} A_p^i \, u^p \right\| \tag{6}$$

where A_p is the p^{th} component of the eigenvector λ^icorresponding to from (3.3) and the discrete 2-norm is defined as

$$\|y\| = \sqrt{y_1^2 + y_2^2 + y_3^2 \ldots y_M^2} \tag{7}$$

The eigenvectors are orthogonal and the eigenvalues are real and non-negative because of the self-adjoint and non-negative properties of the auto-covariance matrix.

Each snapshot can be expressed as a series of the POD modes with coefficients a; for each POD mode i. These POD coefficients are determined by projecting the fluctuating part of the spray onto the POD modes

$$a^n = \psi^T u^N \; n = 1,2, \ldots \ldots . . N \tag{8}$$

Where $\psi = [\, \phi^1 \, \phi^2 \quad \ldots . \phi^N]$ has been introduced. The expansion of the fluctuating part of a snapshot n is

$$u^n = \sum_{i=1}^{N} a_i^n \phi^{'} = \psi a^n \tag{9}$$

Fukunga showed that the total energy from the fluctuations in the snapshot that is associated with a given POD mode is proportional to the corresponding eigenvalue

Therefor the ordering of the eigenvalue and eigen value that the most important modes in terms of energy contribution are the first modes. This usually means that the first modes will be associated with large scale structure. If a flow has dominant flow structures. These are reflected in the first pod modes. Hence a given snapshot can often be reconstructed satisfactorily using only the few modes. The pod analysis caried out in this thesis has m =240, n=240 and N=1000 as the image parameters.

3. Results and discussion

The Proper Orthogonal Decomposition (POD) is a powerful technique for identifying coherent structures in flows, with each POD mode representing a dominant spatial structure that contributes varying levels of energy to the overall flow dynamics. Figure 3 presents the first ten POD modes for q=15, at atmospheric pressure in a jet-crossflow configuration. The first mode captures the largest-scale coherent structures in the jet, primarily governed by shear layer instability at the interface with the crossflow. Large vortex rings and shear layer roll-ups are evident, alongside core jet penetration and crossflow interaction, with high-energy structures suggesting Kelvin-Helmholtz (KH) instability. As the modes progress, secondary instabilities begin to emerge. Mode 2 reveals flow asymmetries and secondary instabilities in the shear layer roll-up, with slight tilting of structures indicating the presence of counter-rotating vortices and the onset of smaller-scale instabilities. Mode 3 captures the interaction between large vortices and the jet core, where vortex stretching becomes prominent and the jet column starts to fragment into smaller vortical structures. The KH instability evolves into a more chaotic turbulent state, enhancing mixing through vortex pairing. By Mode 4, the jet column undergoes noticeable deformation, with coherent vortex cores breaking into filaments and instabilities migrating toward the wake region, indicating interactions with the downstream crossflow wake. The transition to turbulence becomes more evident in Mode 5, which represents the breakdown of the shear layer and the onset of turbulence transition. Large-scale structures from previous modes disintegrate into finer vortices, and the shear layer loses coherence, marking the progressive onset of turbulence, with spanwise vortex stretching becoming visible. In Mode 6, secondary and tertiary instabilities dominate, leading to further fragmentation of structures and clear evidence of vortex tilting and rotation. This mode signifies the transfer of energy from large coherent vortices to smaller turbulent structures, reflecting the classic energy cascade in turbulent flows. Modes 7 through 10 depict the increasing complexity and randomness of the flow. Mode 7 highlights wake instabilities, where the wake region behind the jet becomes dominant, characterized by Von Kármán-like vortices and strong asymmetry in the downstream structures due to the interaction between the crossflow and jet remnants.

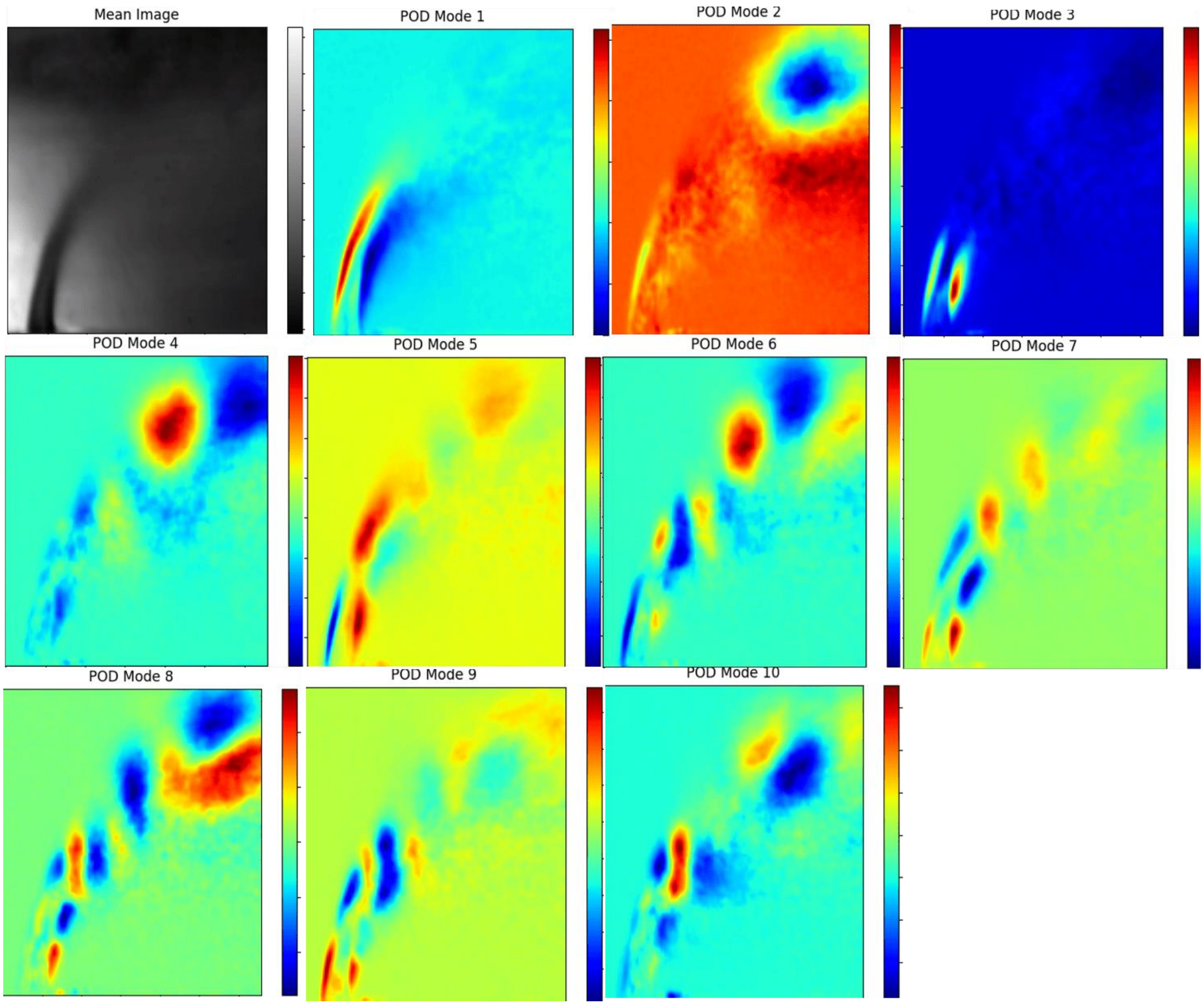

Fig. 3. First ten modes of proper orthogonal decomposition with mean image.

Mode 8 captures fully developed turbulence, where the flow field becomes highly disordered, with the energy cascade fully active and dominated by fine-scale turbulent eddies, representing turbulent dissipation structures. Mode 9 exhibits weakly coherent structures, with small wave-like fluctuations indicative of low-energy flow remnants, where some localized vortices persist but with diminished strength. By Mode 10, the flow becomes almost entirely chaotic and highly fragmented, with no clearly defined structures remaining, only high-frequency oscillations representing background turbulence. As the mode number increases, the energy contribution decreases, transitioning from large-scale coherent structures in the initial modes to fine-scale turbulent fluctuations in higher modes. This progression highlights the energy cascade mechanism and the development of turbulence in the jet-crossflow interaction, where large vortices break down into smaller eddies, leading to a fully developed turbulent state further downstream.

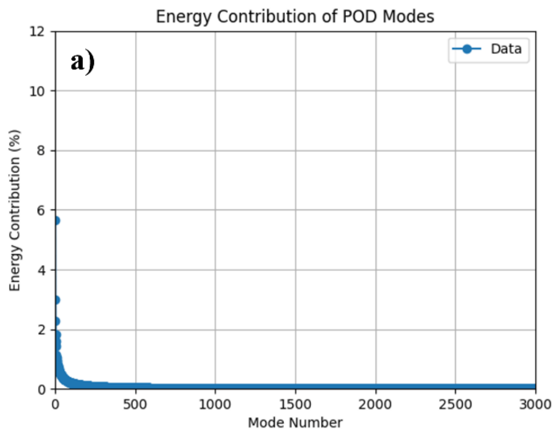

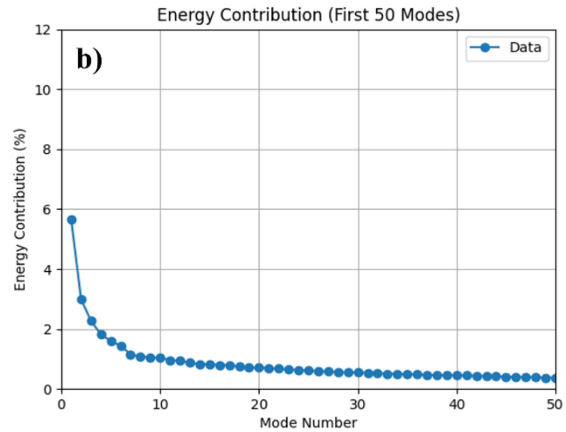

Fig. 4. Contribution of modes a) and, b) for first 50 modes.

Figure 4 illustrates the percentage of energy contribution across different POD modes. Figure 4(a) presents the energy distribution for all 3000 modes, while Figure 4(b) focuses on the first 50 modes to provide a clearer understanding of their contribution. The energy contribution declines rapidly as the mode number increases, highlighting that only a limited number of modes are responsible for capturing the dominant flow structures. Mode 1 exhibits the highest energy contribution, representing the most dominant coherent structure, which is likely the large-scale vortex system in the jet shear layer. Modes 2–5 still retain a significant portion of the energy, corresponding to secondary instabilities such as vortex pairing, stretching, and jet-core interactions. However, beyond Mode 10, the energy contribution becomes minimal, indicating that only the first few modes contain physically meaningful flow structures, while the higher modes predominantly represent fine-scale turbulence. As the mode number increases further, approximately beyond 50–100 modes, the energy levels out, implying that modes in the range of 100 to 3000 primarily account for noise and small-scale turbulent fluctuations. The majority of the energy is captured within the first 10–50 modes, suggesting that low-order reconstructions of the jet flow using only these modes can still effectively capture the key coherent structures without requiring the full 3000-mode spectrum. The dominance of the first few modes in the energy spectrum confirms that the jet in crossflow contains strong coherent structures in its initial evolution. While higher-order modes (above 50–100) contribute very little energy, they remain essential for accurately resolving turbulent dissipation and chaotic fluctuations. If the flow reconstruction is limited to only a few dominant modes, the large-scale vortices will be retained, but finer turbulence details will be lost. Therefore, while a small number of modes are sufficient to represent the primary flow features, capturing the full turbulence spectrum requires incorporating higher-order modes to resolve the fine-scale structures and turbulent dissipation mechanisms. Figure 5 presents the temporal coefficients for the first six POD modes at q=15 under atmospheric conditions, illustrating how each mode's contribution fluctuates over time. These time-series signals provide insight into the dynamic behavior of coherent structures in the jet-crossflow interaction. Higher amplitude values indicate a stronger influence of a particular mode at specific times, revealing the evolution of turbulence and energy distribution across different scales. POD Mode 1 exhibits the highest amplitude range (~ ±750 to ±1000), capturing the most dominant, low-frequency coherent structures. This mode primarily represents large-scale vortex structures in the shear layer, characterized by slow, strong oscillations. POD Mode 2 has a lower amplitude (~ ±400 to ±600) than Mode 1, but begins to capture shear layer instabilities, leading to the development of secondary vortical structures. The oscillations in this mode appear at a higher frequency, indicating the onset of more dynamic fluctuations compared to Mode 1. POD Mode 3, with an amplitude similar to Mode 2 (~ ±400 to ±600), represents weaker but still significant coherent structures, likely associated with vortex pairing and flow interactions. The presence of higher frequency content suggests increased flow unsteadiness, highlighting the transition to smaller-scale turbulence. POD Mode 4 exhibits a further decrease in amplitude (~ ±300 to ±500), indicating the presence of weaker vortices and turbulence transition features. The fluctuations become more random, marking the progressive breakdown of coherent structures into turbulent eddies. As the mode number increases, POD Mode 5 shows a further reduction in amplitude (~

±200 to ±400), representing the onset of smaller-scale turbulence. The flow structures become more fragmented and less periodic, signifying the energy cascade from larger coherent vortices to finer turbulence scales. POD Mode 6, with the lowest lowest amplitude (~ ±100 to ±300), is dominated by small-scale turbulence and fine-scale eddies. The oscillations appear more chaotic and less periodic, confirming the presence of high-frequency turbulence effects

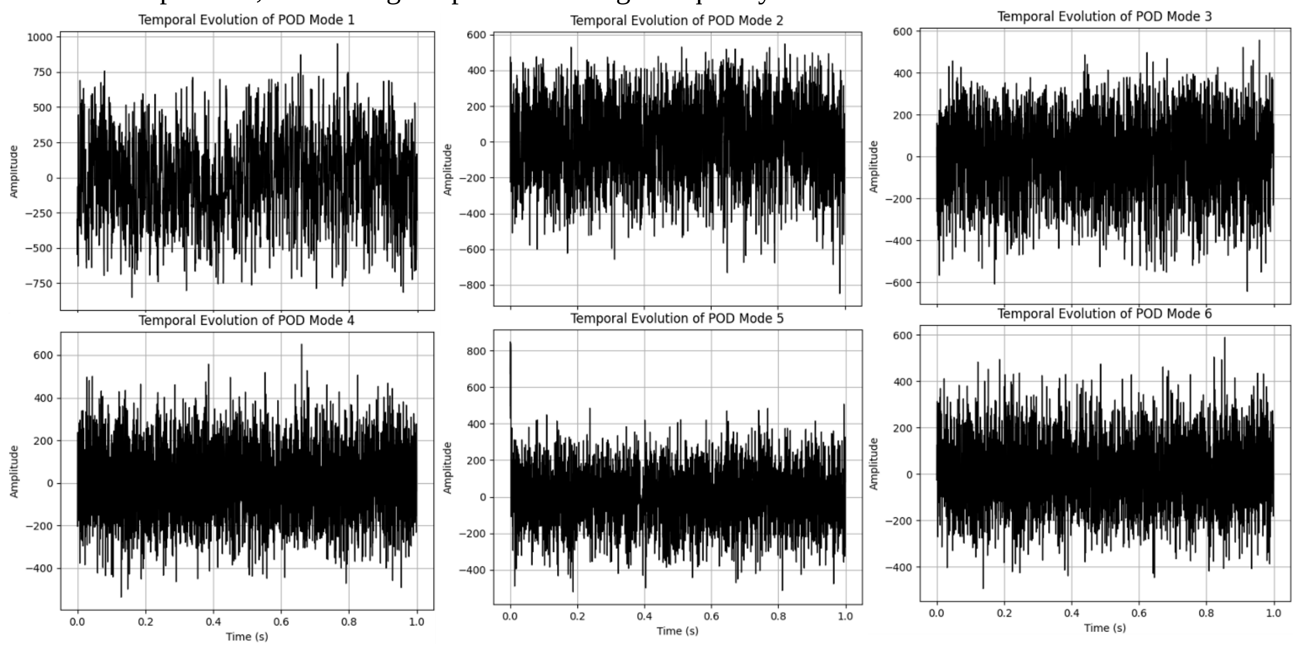

Fig. 5. Time temporal coefficient for first six modes for q=15 at atm. condition.

The trends observed in the temporal coefficients align with the POD energy spectrum from the first 3000 modes. The first few modes (1–6) account for most of the total energy, and their decreasing amplitude reflects the energy distribution trend, where higher modes contribute progressively less energy. When linked to the spatial POD modes from the first 50 modes, these temporal coefficients describe the dynamic evolution of different flow structures. Modes 1–3 correspond to large-scale, coherent vortex structures, while Modes 4–6 transition toward smaller-scale turbulence. Mode 1 dominates the global flow dynamics, exhibiting the largest and slowest oscillations, which represent the primary coherent structures governing jet-crossflow interaction. Higher modes, however, feature more chaotic and higher-frequency fluctuations, indicating the breakdown of large structures into finer turbulence scales. This follows the classical turbulence energy cascade, where energy is progressively transferred from large vortices to small-scale eddies, ultimately leading to a fully developed turbulent flow. Figure 6 presents the Proper Orthogonal Decomposition (POD) modes for different momentum flux ratios (q), arranged in four columns. Each column corresponds to a specific momentum flux ratio, illustrating how the dominant coherent structures evolve as q increases. The first column represents 4q=4 (low momentum flux ratio), the second column corresponds to q=8 (moderate momentum flux ratio), the third column displays q=18 (high momentum flux ratio), and the fourth column shows q=24 (very high momentum flux ratio). Each column contains three POD modes (Mode 1, Mode 2, and Mode 3), providing insight into the development of coherent structures, vortex dynamics, and turbulence evolution. As q increases, the jet exhibits higher penetration into the crossflow, stronger coherent vortices, and delayed turbulence breakdown, demonstrating the transition from a crossflow-dominated regime to a jet-dominated regime. At low q (e.g., 4), the jet is strongly influenced by the crossflow, leading to early turbulence formation and strong shear-layer instabilities.
Mode 1 shows significant jet bending, indicating low penetration and dominant shear-layer roll-up. Mode 2 captures wake instabilities and early turbulence, while Mode 3 reveals fine-scale turbulence structures, signifying rapid breakdown. As the momentum flux ratio increases to q=8, the jet exhibits stronger penetration into the crossflow, with more organized vortex roll-up and Kelvin-Helmholtz instability. Mode 1 highlights a more structured jet column, Mode 2 captures vortex pairing and stretching, and Mode 3 reveals wake interactions that persist further downstream. This suggests that at moderate q, the

jet and crossflow effects are more balanced, leading to strong coherent vortices and a delayed transition to turbulence. At higher momentum flux ratios (q=18), the jet resists bending and remains more intact, forming large-scale Kelvin-Helmholtz vortices that persist longer

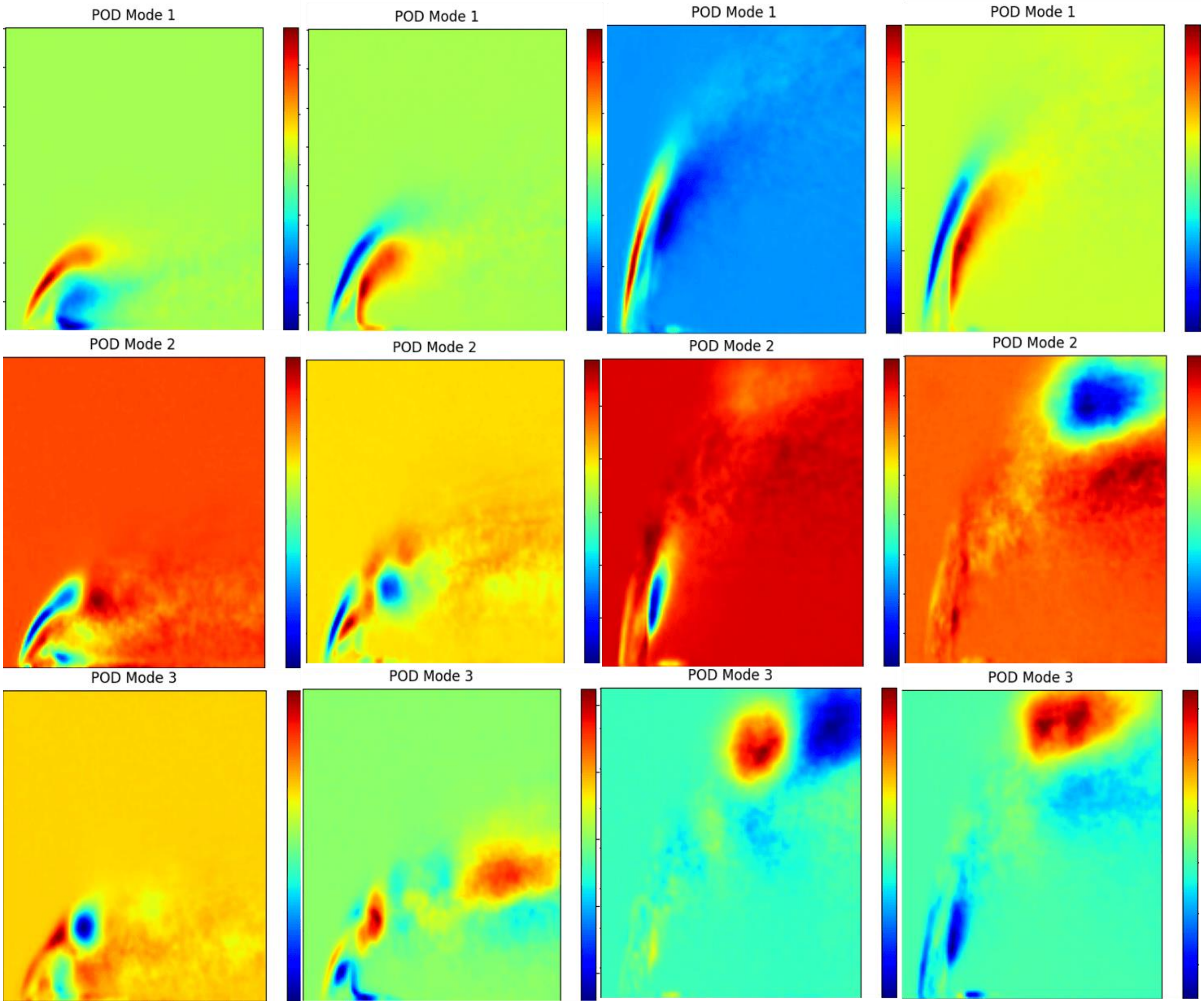

Fig. 6. First three modes for a) q=4, b) q=8, c) q=18 and, 4) q=24.

Mode 1 captures these dominant vortical structures, while Mode 2 showcases vortex stretching and pairing, further delaying turbulence transition. Mode 3 demonstrates that turbulence still forms but at a much later stage, with weaker wake turbulence compared to lower q. At very high q=24, the jet behaves almost like a free jet, with minimal crossflow influence. Mode 1 confirms the jet's strong penetration and coherence, while Mode 2 highlights that shear-layer breakdown is the primary driver of turbulence rather than crossflow interaction. Mode 3 shows fine-scale turbulence structures, representing high Reynolds number effects where self-induced turbulence dominates. Overall, increasing q shifts the flow behavior from a crossflow-dominated regime at low q, where shear-layer instabilities drive turbulence, to a jet-dominated regime at high q, where turbulence is primarily self-induced. At low q, instabilities develop rapidly, leading to early turbulence formation and strong wake interactions. At moderate q, vortex roll-up and coherent structures persist longer, delaying turbulence breakdown.

At high q, the jet retains its structure for a much longer distance, resisting crossflow effects and forming strong Kelvin-Helmholtz vortices. Finally, at very high q, the jet behaves almost independently of the crossflow, with turbulence primarily driven by shear-layer instabilities rather than external forces. This analysis highlights how the momentum flux ratio significantly influences jet dynamics, vortex evolution, and turbulence characteristics in a jet-crossflow crossflow interaction. Examining Figure 7, which presents the temporal coefficients for Mode 1 and Mode 2 across across different momentum flux ratios (q)—specifically q=4, q=8, q=18, and q=24—provides insight into the time-time-dependent behavior of the dominant flow structures. These time-series signals illustrate how the contribution contribution of each mode fluctuates over time, revealing the impact of increasing jet momentum relative to the crossflow on flow stability, vortex dynamics, and turbulence evolution. At q=4 (low momentum flux ratio, crossflow-dominated flow), Mode 1 exhibits lower amplitude variations, indicating weaker coherent structures. The flow is governed by shear-layer instabilities, which lead to early turbulence formation. The fluctuations are high-frequency, signifying rapid vortex breakdown. Mode 2 displays even higher frequency oscillations, suggesting that turbulence intensifies quickly. This mode primarily represents small-scale wake turbulence, as the jet is highly influenced by the crossflow. Due to its low penetration, the jet experiences strong vortex dissipation in the wake region, resulting in early loss of coherence. At q=8 (moderate momentum flux ratio, balanced jet-crossflow interaction), Mode 1 exhibits larger fluctuations compared to q=4, indicating stronger coherent vortices. The presence of some periodicity suggests more organized vortex roll-up. Mode 2 captures vortex pairing and interactions, leading to a slower transition to turbulence. The higher energy fluctuations indicate sustained vortex coherence, with the jet penetrating deeper into the crossflow. Kelvin-Helmholtz instability dominates, delaying turbulence onset compared to lower. At q=18 (high momentum flux ratio, jet starts to dominate), Mode 1 displays even greater amplitude fluctuations, reflecting strong vortex stretching as the jet resists crossflow effects. Large-scale structures persist for a longer duration, delaying turbulence breakdown. Mode 2 captures the transition to turbulence further downstream, where strong fluctuations indicate a delayed vortex breakdown. At this stage, the jet behaves more like a free jet, exhibiting weaker wake interactions, as its higher momentum mitigates crossflow-induced instabilities. The turbulence onset is significantly delayed, allowing for greater jet coherence. At q=24 (very high momentum flux ratio, jet-dominated flow), Mode 1 displays extremely strong and frequent oscillations, indicating self-induced turbulence. The crossflow has minimal impact on the jet's initial behavior, as the jet possesses sufficient momentum to maintain its structure. Mode 2 exhibits intense small-scale fluctuations, representing shear-layer breakdown rather than crossflow-driven instabilities. This suggests that turbulence is entirely self-sustained, with breakdown occurring within the jet's shear layer rather than due to crossflow interactions. At this high q, the jet behaves almost independently of the crossflow, with turbulence being primarily dictated by internal jet instabilities. Overall, the temporal coefficients in Figure 7 reveal a progression from crossflow-dominated turbulence at low q to self-induced turbulence at high. At low q, turbulence is initiated by shear-layer instabilities and amplified by crossflow interactions, leading to early breakdown. At moderate q, vortex pairing and Kelvin-Helmholtz instability enhance vortex coherence, delaying turbulence onset. At high q, jet momentum dominates, suppressing wake instabilities and postponing turbulence transition. Finally, at very high q, the jet behaves almost like a free jet, where turbulence is governed primarily by internal shear-layer breakdown rather than external crossflow effects. This evolution highlights the increasing dominance of jet momentum over crossflow forces, significantly altering the dynamics of vortex interactions and turbulence development.

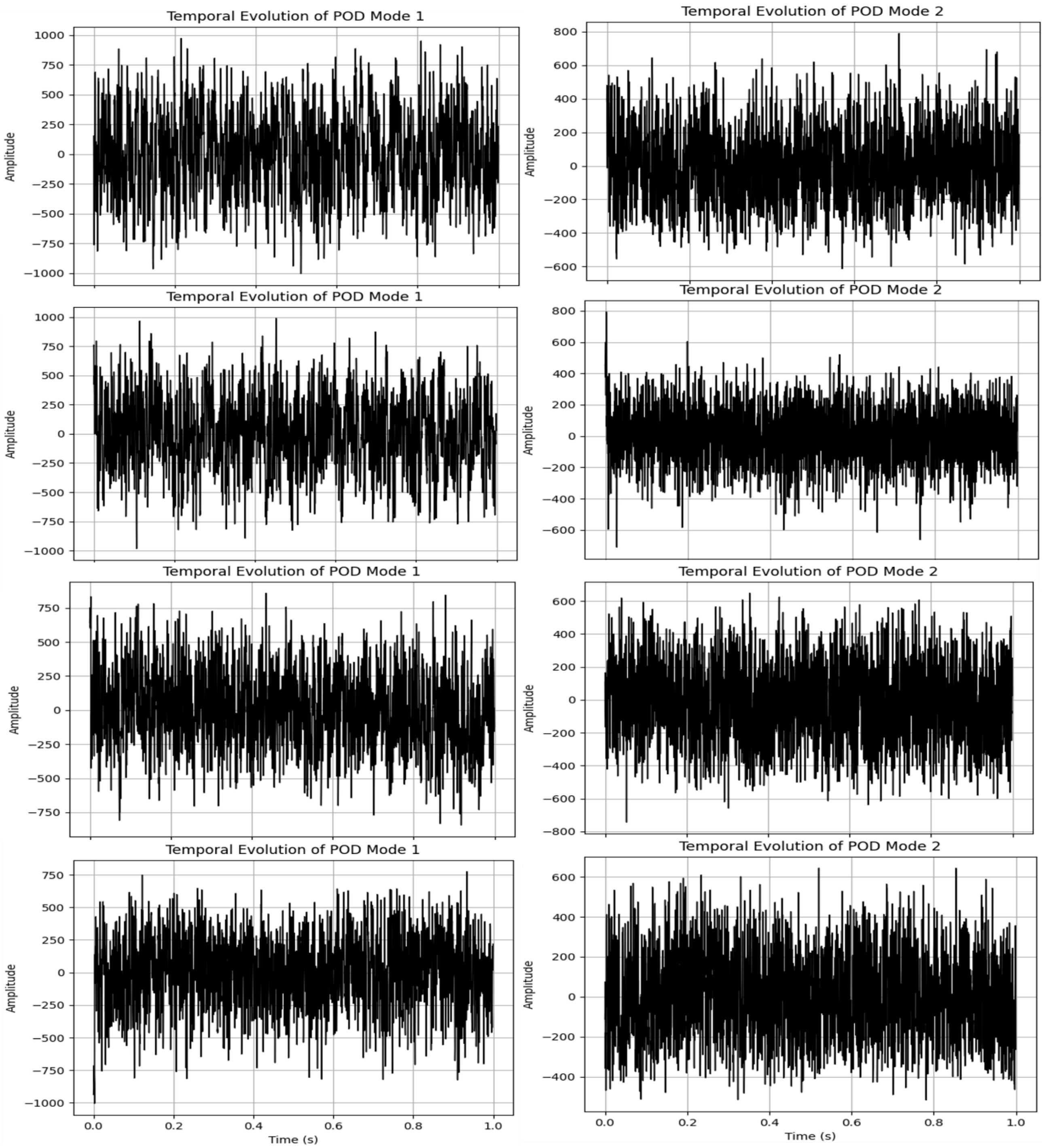

Fig. 7. Temporal coefficient for mode 1 and 2 for a) q=4, b) q=8, c) q=18 and, 4) q=24.

4. Conclusion

TThis study employs Proper Orthogonal Decomposition (POD) to analyze the coherent structures, energy distribution, and temporal evolution of a jet in crossflow at different momentum flux ratios (q). The results reveal that the first few POD modes capture the dominant large-scale structures, while higher modes represent fine-scale turbulence and dissipation. At low q, the jet is strongly influenced by the crossflow, leading to early turbulence formation driven by shear-layer instabilities. As q increases, vortex roll-up and coherent structures persist longer, delaying turbulence onset. At high q, the jet maintains its integrity over a longer distance, forming strong Kelvin-Helmholtz vortices, with turbulence transition occurring further downstream. At very high q, the jet behaves almost independently of the crossflow, with turbulence primarily driven by internal shear-layer instabilities rather than external interactions.

The energy spectrum confirms that a small number of modes effectively capture the primary flow structures, with the first 10 containing most of the energy. Temporal analysis further illustrates the evolution of coherent structures, showing a shift from crossflow-dominated turbulence at low q to self-sustained turbulence at high q.

Acknowledgements

The author would like to acknowledge Pratt & Brittney USA for financial support.

References

[1] Wu, X., Fuller, R. P., Kirkendall, K., & Nejad, A. S. (1997). Liquid jet breakup in crossflow: Surface breakup and penetration dynamics. *Journal of Fluid Mechanics*, 336, 1-30.

[2] Taylor, G. I. (1950). The instability of liquid surfaces when accelerated in a direction perpendicular to their planes. *Proceedings of the Royal Society of London. Series A, Mathematical and Physical Sciences*, 201(1065), 192-196.

[3] Wu, X., Fuller, R. P., & Kirkendall, K. (1997). Measurements of droplet size and velocity in spray plumes. *Experiments in Fluids*, 23(2), 140-156.

[4] Vich, M. (1997). Experimental studies on liquid jet primary breakup in crossflow. *AIAA Journal*, 35(7), 1123-1130.

[5] Mazallon, J., Zhu, J., & Faeth, G. M. (1999). Primary breakup of turbulent liquid jets in gas crossflows. *International Journal of Multiphase Flow*, 25(8), 1535-1545.

[6] Sallam, K. A., Aalburg, C., & Faeth, G. M. (2002). Breakup of round nonturbulent liquid jets in gaseous crossflow. *AIAA Journal*, 40(3), 451-460.

[7] Kush, J. & Schetz, J. (2000). Liquid jet injection into supersonic crossflows. *Journal of Propulsion and Power*, 16(4), 576-582.

[8] Ingebo, R. D. (1980). Atomization of liquid jets in crossflows: Effects of capillary and acceleration waves. *NASA Technical Report*, 1205.

[9] Schetz, J. A., & Padhye, R. (1993). Momentum analysis of maximum penetration heights for liquid jets in crossflow. *Journal of Fluids Engineering*, 115(3), 423-429.

[10] Nejad, A. S., & Schetz, J. A. (1996). Effects of liquid properties on penetration heights in supersonic crossflows. *AIAA Journal*, 34(8), 1785-1793.

[11] Chen, Y., Heister, S. D., & Crowe, C. T. (1998). Experimental investigation of jet trajectories and spray regimes using Mie scattering. *Journal of Propulsion and Power*, 14(2), 162-170.

[12] Thomas, L., & Schetz, J. A. (1995). Spray characteristics of liquid jets in supersonic airstreams. *International Journal of Multiphase Flow*, 21(3), 377-394.

[13] Sankarakrishnan, S., & Sallam, K. A. (2008). Experimental study of Rayleigh-Taylor instability in non-turbulent liquid jets undergoing bag breakup. *Physics of Fluids*, 20(4), 042101.

[14] Lumley, J. L. (1967). The structure of inhomogeneous turbulence. *Atmospheric Turbulence and Radio Wave Propagation*, 166-178.

[15] Sirovich, L. (1987). Turbulence and the dynamics of coherent structures. Part I: Coherent structures. *Quarterly of Applied Mathematics*, 45(3), 561-571.

[16] Bernero, S., & Fiedler, H. (2000). Application of PIV and POD to the study of coherent structures in turbulent flows. *Experiments in Fluids*, 29(1), 274-281.

[17] Wu, X., Kirkendall, K., Fuller, R. P., & Nejad, A. S. (1997). High-speed imaging of liquid jet breakup in crossflow. *Journal of Fluids Engineering*, 119(2), 340-350.